Self-organized Criticality in Neuromorphic Nanowire Networks With Tunable and Local Dynamics

ADVANCED FUNCTIONAL MATERIALS
www.afm-journal.de

Self-organized Criticality in Neuromorphic Nanowire Networks With Tunable and Local Dynamics

Fabio Michieletti, Davide Pilati, Gianluca Milano, and Carlo Ricciardi**

Self-organized criticality (SOC) has attracted large interest as a key property for the optimization of information processing in biological neural systems. Inspired by this synergy, nanoscale self-organizing devices are demonstrated to emulate critical dynamics due to their complex nature, proving to be ideal candidates for the hardware implementation of brain-inspired unconventional computing paradigms. However, controlling the emerging critical dynamics and understanding its relationship with computing capabilities remains a challenge. Here, it is shown that memristive nanowire networks (NWNs) can be programmed in a critical state through appropriate electrical stimulation. Furthermore, multiterminal electrical characterization reveals that network areas can establish spatial interactions endowing *local* critical dynamics. The impact of such tunable and local dynamics versus the information processing in the network is experimentally analyzed through in materia implementation of nonlinear transformation (NLT) tasks, in the framework of reservoir computing. As for brain where cortical areas are specialized for a certain function, it is demonstrated that the computing performance of nanowire networks rely on the response of reduced subsets of outputs, which may show critical dynamics or not, depending on the specificity of the task. Such brain-like behavior can lead to neuromorphic systems based on self-organizing networks with reduced hardware complexity by exploiting their local and specialized behavior.

1. Introduction

Self-organized criticality (SOC) is a recurrent property in nature for a multitude of complex phenomena.[1–3] In particular, a crucial role in biological neural systems is demonstrated.[4] Through experimental recordings of local field potential (LFP), evidence of SOC emergence has been reported in cortical neuron cultures and cerebral cortex for animals and humans, in addition to the amygdala and hippocampus for the latter.[5–11] Although these observations are not sufficient to undoubtedly assess the role of criticality in brain information processing, parallel motivations to bio-plausibility have driven the study of SOC in dynamical systems.[12] When poised to the critical state, it has been argued that dynamical systems maximize processing performance in terms of dynamic range, information storage and transmission, computational power, and stability.[6,13–19] In this framework, SOC has been explored in emerging hardware technologies for computing, including self-organizing systems such as nanowires, nanoparticles, and nanogranular networks, where the complex interaction among a multitude of nanometric nonlinear elements inherently enables the arising of this emergent phenomenon.[20–31] Among self-organizing systems, memristive nanowire (NW) and percolating nanoparticle networks have been confirmed, both experimentally and in simulations, to show critical dynamics in response to two-terminal voltage stimulation and reading.[20,25,27,32,33] At the same time, the emergent dynamics of these systems have been exploited for the implementation of physical reservoir computing (RC).[34–37] For this application, it has been argued through simulations that criticality can provide a progressive performance boost with the increasing task complexity and required memory, along with experimental observations of a detrimental effect for simpler tasks.[32,38] However, controlling the emerging critical dynamics and understanding its relationship with computational properties in experimental systems remains a challenge.

In this work, we report on self-organized criticality in neuromorphic NW networks (NWNs), demonstrating the possibility of programming the network to a critical state through proper electrical stimulation. By manipulating the electrical connectivity of the system, we show that the network can be posed in a conductance state characterized by switching events satisfying criteria for criticality. By demonstrating in a multiterminal configuration that interactions between local network areas can show

F. Michieletti, D. Pilati, C. Ricciardi
Department of Applied Science and Technology
Politecnico di Torino
Turin 10129, Italy
E-mail: carlo.ricciardi@polito.it
D. Pilati, G. Milano
Advanced Materials Metrology and Life Sciences Division
Istituto Nazionale di Ricerca Metrologica
Turin 10135, Italy
E-mail: g.milano@inrim.it
The ORCID identification number(s) for the author(s) of this article can be found under https://doi.org/10.1002/adfm.202423903

DOI: 10.1002/adfm.202423903

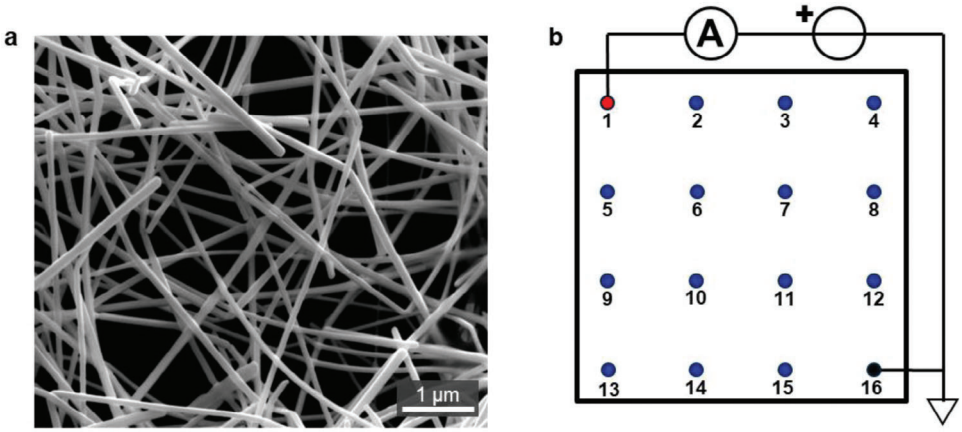

Figure 1. NWN microstructure and electrical characterization. a) Scanning Electron Microscope (SEM) image of the complex network structure. b) Schematic reproduction of the multiterminal setup. Electrode 16 (black dot) is set as voltage reference and the stimulating signal is applied to terminal 1 (red dot). Locations 2 – 15 are contacted to floating voltage probing electrodes (blue dot).

spatially distributed critical dynamics, we move beyond the classical evaluation of the global criticality of the system through two-terminal measurements. We demonstrate that local critical dynamics can arise also in devices that do not show global criticality. Furthermore, we experimentally show that such a *local* criticality, which is observed in the interaction among network areas characterized by specific activation properties, is correlated with nonlinear transformation properties of the network, as experimentally analyzed through the implementation of nonlinear transformation (NLT) computing tasks. By exploiting characteristic nonlinear response and critical behavior of network areas, we show that a specific subset of electrodes mainly contributes to the accuracy of the system depending on the specific target waveform. These results are of important for deepening the understanding of how to drive a self-organizing system in a critical regime, as well as for the proper selection of output features and operating conditions of reservoir systems, toward a network with task-oriented areas. This behavior resembles the different specificity that cortical areas develop in the brain upon experience.

2. Results and Discussion

2.1. Memristive Behavior of Ag NW Networks

Memristive nanowire networks were produced by drop-casting a solution of Ag NWs onto an insulating substrate (**Figure 1**a, Experimental Section), as detailed elsewhere.[39,40] A detailed analysis of structural and electrical properties of Ag NWs reported in our previous work[39] revealed that NWs are characterized by a crystalline structure and are surrounded by an amorphous and insulating polyvinylpyrrolidone (PVP) shell layer of ≈1–2 nm. The presence of this PVP shell layer directly results from the polyol synthesis of Ag NWs, where this polymer is exploited as a surfactant to control the NW morphology.[41,42] These NW networks endow an emergent memristive behavior that arises from resistive switching effects in NWs and NW junctions, as experimentally investigated in previous works.[39,43] In particular, each intersection between nanowires forms a Ag/PVP/Ag electrochemical memristive cell, which confers to the network a nonlinear response to electric stimulations and a short-term plasticity behavior characterized by pulse-triggered potentiation followed by subsequent spontaneous relaxation.[27,39] The electrical characterization of neuromorphic NWNs is typically performed in two-terminal configuration, by forcing bias and reference voltage to mutually peripheral regions of the sample. The intrinsic system complexity has been demonstrated to give rise to emergent brain-like dynamics such as homo and heterosynaptic plasticity, structural reconfiguration through reweighting and rewiring, paired-pulse facilitation, and engram memory pattern formation.[27,39,47] Criticality in self-organizing memristive networks is linked to the interplay of *i)* network topology and *ii)* the resistance state of each NW junction, both aspects regulating the flow of current through the system. When a resistive switching event occurs in a single NW junction, consequent changes in the electric field and current across other junctions occur, causing further resistive switching events in other network areas. Successive switching events lead then to other events, creating an avalanche effect that is related to criticality. While a similar mechanism was proposed to explain criticality in nanoparticle networks with a network topology that lies at the onset of percolation,[25] direct experimental visualization of avalanche effects in networks is difficult to assess since it requires high-resolution visualization of spatially distributed resistive switching events across the whole network. In this context, multiterminal measurements can be exploited to access the spatiotemporal dynamics of these systems[48] (Figure 1b). In this configuration, while electrical stimulation is applied between mutually peripheral bias and ground electrodes (Figure 1b, red and black contacts respectively), additional floating voltage electrodes enable the measurement of the voltage drop (with respect to ground) at specific spatial locations (Figure 1b, blue electrodes). These voltage drops evolve depending on the evolution of the electric field distribution and current flow across the network.

In this way, real-time spatiotemporal dynamics can be tracked through voltage maps. More details about the multiterminal setup for the electrical characterization of NWNs can be found in the Experimental Section and ref. [45].

2.2. Global Network Criticality

The evaluation of criticality in brain-inspired complex systems is commonly performed by investigating the temporal derivative of conductance response to an external constant bias in a two-terminal fashion (i.e. when reading from the same two electrodes/areas that are subjected to bias).[25,32] In this case the system behavior results from the recurrent interaction of its nonlinear junctions structurally connecting stimulated areas, and criticality represents an emergent property of the whole network. Here in this work, two-terminal measurements were performed in between electrodes located in mutually peripheral areas of the sample (electrodes 1 and 16), and we refer to *global* criticality when such configuration is employed.

2.2.1. Example of a Globally Critical Network

The two-terminal dynamical analysis of a NWN showing global criticality is reported in **Figure 2**. Here, dynamic analysis has been performed on a network state characterized by an average effective conductance of $< G > = 0.22\ G_0$ under 100 mV stimulation, where G_0 is the fundamental quantum of conductance $G_0 = 2e^2/h$. Figure 2a shows the NWN conductance derivative signal, where a complex spiking pattern can be observed. Note that the magnitude of the spikes covers a wide range of values, coherently with spatial self-similarity.[46] In this context, a crucial aspect is represented by the disentanglement of the spike activity with the background noise. For this purpose, the criteria for establishing the limit of detection (LOD) separating spiking activity from noise (red line in Figure 2a) have been chosen by identifying the zero-centered interval that better fits a Gaussian distribution for noise (see Experimental section for details). The network dynamical state is investigated by analyzing the statistical properties of events occurrence, where events are identified as the maximum value of each LOD-overcoming consecutive interval.

Events magnitude distribution follows a power-law for more than two orders of magnitude (Supplementary Figure S1, Supporting Information), implying spatial self-similarity. Also, the inter-event interval (IEI) distribution demonstrates a power-law behavior for more than a decade, suggesting temporal scale-free dynamics.[46] Additional confirmation of scale-invariance is observed in the IEI autocorrelation function (ACF) depicted in Figure 2b. It shows a power-law dependence on the time lag for more than 300 s after which a cutoff is observed and ACF drops below the 95% confidence threshold under which a positive value cannot be considered statistically different from zero. Considering that other fractal processes different from SOC can demonstrate autocorrelated inter-event intervals,[47] further confirmation is provided by shuffling IEI values, resulting in the annihilation of any correlation. The successive analysis is performed on the activity pattern. According to neuroscience literature,[5] activity is the result of events binning with identical time intervals of width equal to the average inter-event interval. The resulting pattern is composed of consecutive intervals of nonzero activity called avalanches. At the physical level, each avalanche consists of an activity burst caused by a resistive switching event that triggers a local voltage redistribution and a consecutive switching cascade, until reaching a steady state. This behavior is usually described as a first order autoregression process with the representation expressed in Equation 1:

$$\left\langle A_{t+1} \mid A_t \right\rangle = mA_t + h \tag{1}$$

where $\langle A_{t+1}|A_t\rangle$ is the conditioned probability of observing an event at time $t+1$ given the activity at time t, m is the branching parameter, and h is the driving input.[47]

For a critical system, it is required that $h = 0$ and $m = 1$.[49] When an external voltage is applied, the former condition is satisfied only if the system does not show any spontaneous activity, as in the case of NW networks. The experimental estimation of m is typically a difficult task for complex systems, because of the limitation in the number of electrodes available for spatially probing the activity. Indeed, it causes the impossibility of detecting some events that do not occur in their proximity (spatial subsampling). Therefore, a subsampling-invariant estimation is performed by evaluating the ACF of the activity pattern. Indeed, Wilting et al.[48] demonstrated that the autocorrelation function must follow an exponential decay in time directly related to m value, as shown in Equation 2:

$$ACF_k \sim \quad m^k = e^{-\frac{k\Delta t}{\tau_{corr}}} \tag{2}$$

where Δt is the timeframe of the activity characteristics, k is the number of Δt multiples underlying the lag and τ_{corr} The autocorrelation exponential decay time.[48] Figure 2c depicts the experimental activity ACF which shows a clear exponential decay in time with values higher than the 95% confidence line for more than 950 s and $\tau_{corr} = (690 \pm 18)\ s$. The resulting m parameter has a value very close to unity (0.9979 ± 0.0001), providing additional evidence of critical behavior. Also, in this case, the correlation is destroyed by shuffling activity values.

Finally, the statistical assessment of criticality delineated by Sethna et al.[50] and applied in most similar studies is performed. According to this protocol, a critical system must produce avalanches satisfying several statistical requirements that will be detailed in the following. Avalanche sizes (S) and durations (D), which are respectively determined as the total avalanche activity and the number of underlying time bins, must follow the power laws reported in Equations 3 and 4:

$$P(S) \sim S^{-\tau} \tag{3}$$

$$P(D) \sim D^{-\alpha} \tag{4}$$

Figure 2d,e report the respective distributions, which correctly show heavy-tailed behavior for more than a decade with exponents $\tau = 1.85 \pm 0.05$ and $\alpha = 1.89 \pm 0.06$. These values can be combined through the crackling noise relation (Equation 5)

$$\frac{\alpha - 1}{\tau - 1} = \frac{1}{\sigma \upsilon z} \tag{5}$$

obtaining the first evaluation of the so-called critical exponent $1/\sigma\upsilon z = 1.04 \pm 0.06$.

Power-law distributions alone are not sufficient for claiming the system to be critical, but the critical exponents must be validated by performing two additional independent evaluations.

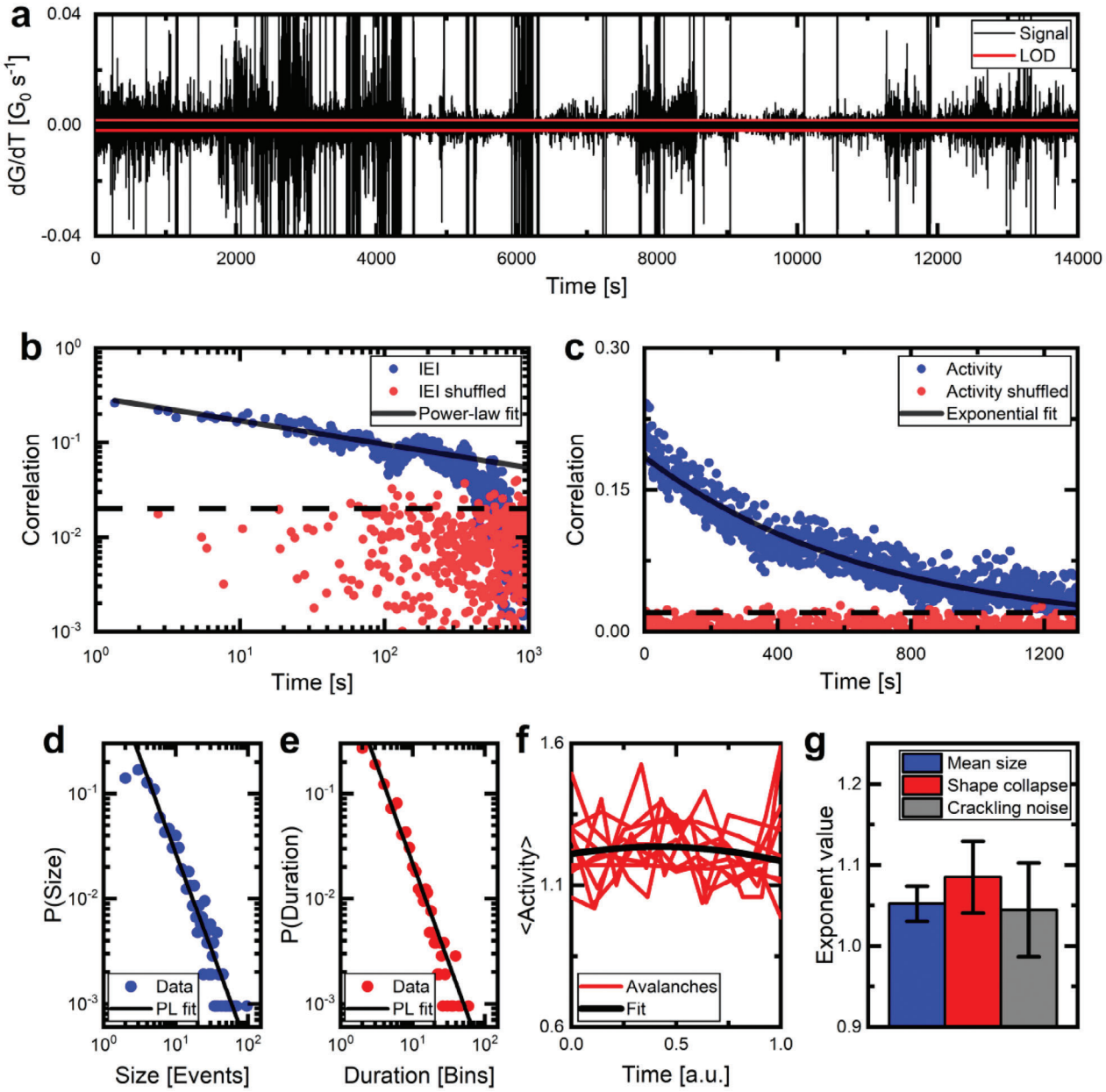

Figure 2. Dynamical analysis of NWN behavior at $< G > = 0.22\ G_0$ under 100 mV constant voltage. a) Conductance time derivative pattern (black) and events LOD (red). b) IEI autocorrelation function (blue dots) showing heavy-tailed behavior for more than two decades and resulting power law fitting (black straight line). Events shuffling results in an ACF (red dots) drop below the 95 % confidence line (black dashed). c) Activity ACF (blue dots) with respective shuffling induced reduction (red dots) below confidence level (black dashed line). The original ACF correctly follows the exponential fit (black straight line) for more than 1000 s. d,e) Heavy-tailed probability density functions of avalanche size (blue) and duration (red) with resulting power-law fittings (black). f) Avalanches showing shape collapse (red) and resulting universal scaling function (black). g) Critical exponents values and respective uncertainties demonstrating full compatibility.

Due to self-similarity, each average avalanche shape for fixed duration $\langle s \rangle(t, D)$ must collapse onto a universal function $F(t/D)$ after normalization of its duration to unity. The critical exponent can be evaluated through the shape collapse according to the transformation shown in Equation 6:

$$F\left(\frac{t}{D}\right) = \langle s \rangle\ (t, D) \cdot D^{1-\frac{1}{\sigma \upsilon z}} \tag{6}$$

Figure 2f shows how experimental avalanches correctly collapse with $1/\sigma\upsilon z = 1.09 \pm 0.04$. Starting from Equation 6, Equation 7 can be derived as:

$$\langle S \rangle\ (D) \sim D^{\frac{1}{\sigma \upsilon z}} \tag{7}$$

which produces the last exponent evaluation. The plot of the relation between mean size and duration is shown in Supplementary

Figure S2 (Supporting Information) and the extrapolated slope results to be $1/\sigma\nu z = 1.05 \pm 0.02$. The compatibility between the critical exponent evaluations (Figure 2g), supported by proper power-law distributions, avalanche shape collapsing, long-range correlations, and branching parameter closeness to unity provide a solid indication of critical dynamics in the NWNs under study. In this context, it is worth noticing that the selection of the LOD plays a crucial role. Indeed, the selection of a too low threshold hinders the possibility of observing fingerprints of SOC. Instead, if the threshold is chosen at too high values, the result is a subsampling of the events. The detrimental effect of a different LOD choice on the statistical analysis of the signal is analyzed in detail in Supplementary Figure S3 (Supporting Information).

2.2.2. Example of a Non-Globally Critical Network

As a comparison, the analysis of an NWN conductance not showing global criticality is reported in **Figure 3**. Here, a network characterized by an average conductance $< G > = 73.38\ G_0$ is analyzed. This state shows a conductance derivative almost fully Gaussian (Figure 3a), with few over-threshold events that do not follow a power-law distribution (Figure S1, Supporting Information). The limited number of spikes causes the 95% ACF confidence interval for IEI (Figure 3b) and activity (Figure 3c) to increase significantly. Consequently, almost all autocorrelation values lie below the significance line, statistically resulting in non-different from zero. This behavior is also confirmed by the negligible ACF variations obtained by shuffling both IEI and activity time series. For these reasons, no spatio-temporal self-similarity can be deduced. Furthermore, the increase in <IEI> causes a reduction in the avalanche population, which makes unreliable the power-law fitting shown in Figure 3d,e. Figure 3f reveals that also avalanche shapes are not in line with the expected standard downward concavity. For all these reasons, the resulting compatibility of the critical exponents shown in Figure 3 g cannot be considered as statistically relevant for assessing criticality.

The observed emergence of global criticality depending on the effective conductance is caused by the variation of functional connectivity underlying different conductive states. In a network with low conductance values, only a few conductive paths are formed, posing it close to the percolation edge.[27,51,52] Here, highly correlated scale-free activity avalanches are expected to emerge, leading to SOC dynamics.[53] Increasing nanowire areal density (*structural* connectivity) and/or inducing the electrical potentiation of the conductance state (*functional* connectivity)[28] force the establishment of several high conductive pathways, resulting in a higher effective conductance of the system, and pushing the NWN above the percolation onset.[28] In this state, the occurrence of switching events and their correlation can be inhibited owing to the strong network connectivity. Indeed, strong electrical potentiation enlarges the size of single junction filaments, conferring high stability and reducing the probability of triggering local resistive switching events at junction levels.[54] Moreover, even if a rare event occurs, the induced voltage redistribution splits between the high number of surrounding elements belonging to the conductive path. Consequently, each individual junction experiences a dumped modulation on the voltage drop at its ends, limiting the switching probability.[27] As a consequence, only a few events are observed, each of which is unable to generate an avalanche.

2.3. Network Programming and Local Criticality

In the previous section, we discussed the principles of criticality assessment applied to a network investigated in a two-terminal configuration. In addition to this *global* criticality, resulting from the whole network dynamics measured from two electrodes, a multiterminal configuration permits the extraction of additional information related to the *local* spatial distribution of critical dynamics. These measurements are performed in a 16-electrode fashion (Experimental section, Figure 1b), where voltage is still applied along the sample diagonal, with bias on electrode 1 and ground on electrode 16, as in the previously discussed two-terminal analysis. Therefore, the current flowing between them can be recorded, permitting the evaluation of the network's global criticality. The information gain of the multiterminal setup is carried by the remaining 14 electrodes that are used for probing the floating voltage distribution over the whole network area without inducing local modifications since no stimulation is applied through them. By applying the criticality analysis to the voltage drop between each couple of floating electrodes, the emergence of local critical dynamics between network areas can be then evaluated. Here in this work, we refer to *local* criticality when such a multiterminal floating electrode configuration is employed, in addition to the standard *global* criticality assessment via two-terminal electrodes. Considering that fluctuations of the differential voltage of a specific electrode pair follow the variation of the network impedance observed from those contact ends, this analysis permits to unraveling of the effect of the overall network dynamics on the interaction between probed areas. In the following, we demonstrate the capability of electrically programming the dynamical state of the NWN to different critical regimes by tuning its two-terminal conductance. The programming protocol consists of forcing a voltage ramp for triggering the desired conductance state, successively sustained by a constant voltage of 1 V for analyzing the dynamics. The selection of the conductance levels is carried out by programming the device in different representative conductance states through voltage ramps. At low voltage, conductance shows stepwise growth, followed by a continuous quasi-linear increase at higher voltage (details on the programmability of conductance states in Supplementary Figure S4, Supporting Information). We selected the states $\langle G_1 > = 0.4\ G_0$, $< G_2 > = 0.81\ G_0$ and $< G_3 > = 1.81\ G_0$ as representative of the first potentiation plateau, the last observed plateau, and the quasi-linear growth, respectively. As shown in Supplementary Figure S3 (Supporting Information), it is worth noticing that after triggering each state with a high voltage forming ramp, these states can be recalled by applying a low voltage ramp, making it possible to reproducibly program the network to the desired effective conductance state.

Figure 4a shows the applied voltage (black line) together with the two-terminal conductance response (blue line) of the network for the state G_1. Green background identifies the programming phase, while the red background is the sustaining one. Figure 4b depicts the time-averaged spatial voltage distribution over the network during the constant bias phase. It results in a conductive

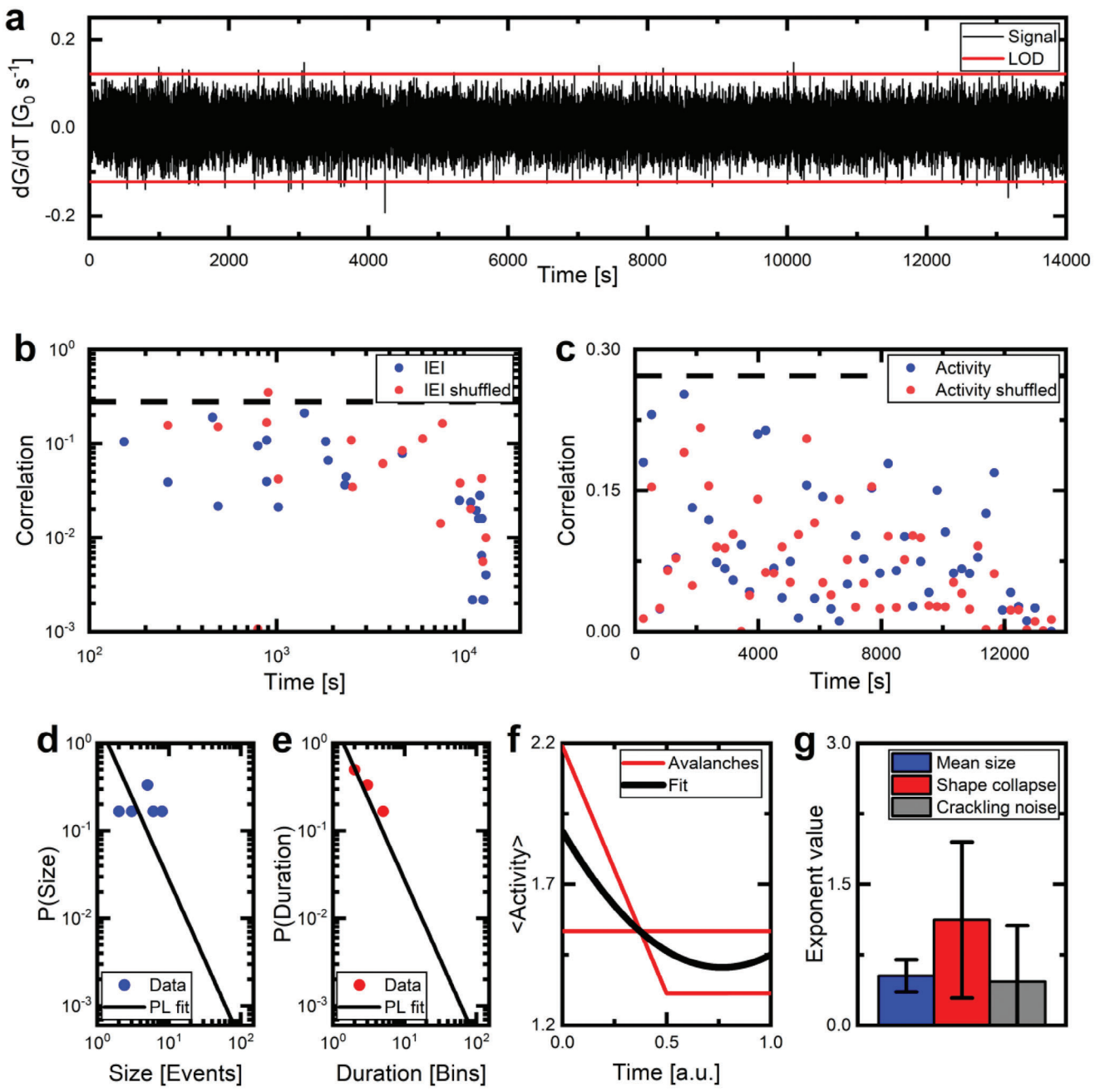

Figure 3. Dynamical analysis of NWN behavior at $< G > = 73.38\ G_0$ under 100 mV constant voltage. a) Conductance time derivative pattern (black) and events LOD (red). b) IEI autocorrelation function (blue dots) underlying the 95% confidence level (black dashed line) and showing superposition with its shuffled counterpart (red dots). c) Activity ACF (blue dots) with respective shuffled version (red dots) and confidence level (black dashed line) demonstrating no statistical relevance as for the IEI ACF. d,e) Probability density functions of avalanche size (blue) and duration (red) which show limited population and scarce adherence to their resulting power-law fittings (black). f) Avalanches shape collapse (red) and resulting universal scaling function (black) show upwards concavity and poor collapsing due to limited population. g) Critical exponents values and respective uncertainties which show compatibility statistically not relevant.

path connected to a bias electrode (top-left) and mainly formed in the bottom-left sample region (testified by the nearly equipotential adjacent areas). Figure 4c reports the resulting criticality matrix, where the *ij*-th element represents the assessment of self-organized criticality on the differential signal between floating voltage electrodes *i* and *j* following the same criteria used for the two-terminal conductance study of Figure 2, together with the bar plot highlighting the total number of critical connections that each electrode area establishes. Despite the difference in the nature of the studied signal, any variation in the voltage difference is proportional to the variation in the network resistance seen by the ends of the specific electrode couple. This means that the

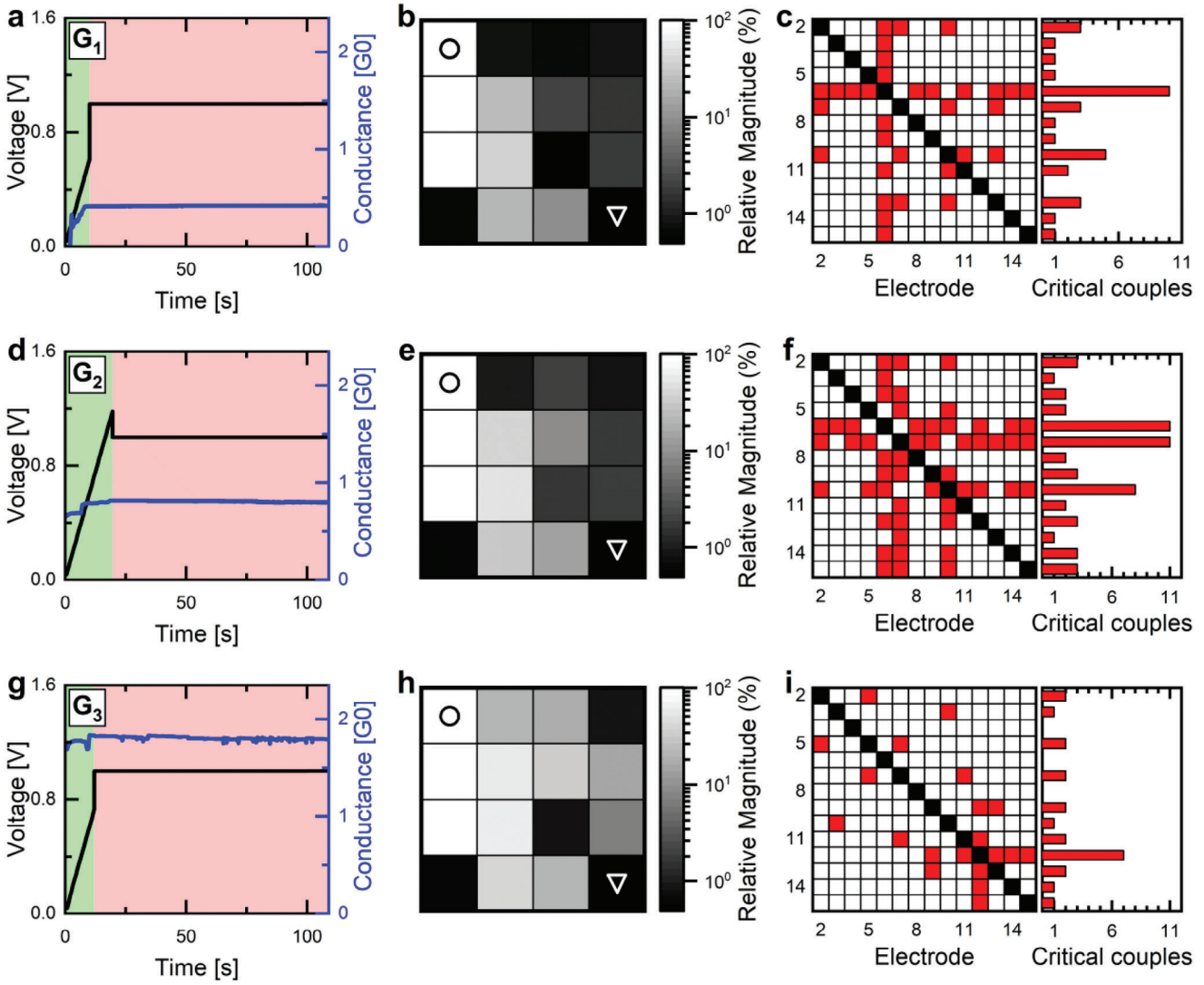

Figure 4. NWN multi-state programming. a,d,g) Two-terminal applied voltage (black line) and conductance response (blue line) during state selection for G_1, G_2, and G_3 states, respectively. The green background identifies the programming phase, while the red background is the sustaining one. b,e), h) Corresponding NWN voltage distributions, evaluated as the average of the voltage read during the sustaining phase for each electrode. The reference electrode is marked with a white triangle and the bias one with a black circle. A conductive path connected to the bias electrode is formed in the bottom-left sample region, while the top-right area progressively activates with conductance growth. c,f,i) Criticality matrices (left panel) and total number of critical relations established by each electrode (right panel). State G_2 demonstrates the maximum number of critical couples, the whole involving electrodes located at the transition between high and low voltage areas.

statistical properties studied for the criticality assessment (distribution trends and autocorrelations) are preserved when changing the measurement from current to voltage. For the sake of completeness, criticality matrixes for bias and ground are shown in Supplementary Figure S5 (Supporting Information). State G_1 exposes critical connections involving electrodes 6 and 10 with accumulation on electrode 6. Note that these specific areas are mainly found in the sample central region, across the diagonal forcing bias, and at the transition between high and low conductive regions. The occurrence of a stepwise transition from G_1 to G_2 (Figure 4d) is associated to the partial creation and reinforcement of electrical connections between bias electrode and the network top-right area (Figure 4e), coherently with the parallel formation of conductive pathways discussed at the end of Section 2.1. The number of SOC interactions (Figure 4f) increases significantly, with a particular effect on electrode 7, whose voltage grows to a level compatible with electrode 6. Furthermore, each of the other electrodes establishes a critical connection with electrodes 6 or 7, spanning the whole network area. In the quasi-linear potentiation regime (state G_3, Figure 4g), the network exhibits an almost symmetric voltage distribution (Figure 4h) caused by the full formation of secondary paths connecting bias and ground electrodes and/or by the enlargement of the existing ones. Focusing on electrode 11, where null voltage is read in state G_1, it undergoes partial activation in G_2 and turns off again in G_3. This fluctuation evidences the tentative formation of a

connectivity configuration with high conduction in this region followed by a successive rearrangement to the most stable one reached in G_3. The criticality matrix (Figure 4i) loses the patterns observed in the previous G_2 state, undergoing a significant reduction of the critical connections number, with slight accumulation on electrode 12 which is found at the transition between the highly conductive top region and the poorly conducting bottom one.

To unveil the relation between global and local criticality, the global criticality assessment was also performed on the two-terminal conductance of each programmed state and reported in Supplementary Figures S6, S7, and S8 (Supporting Information). Although the analysis of G_1 and G_3 reveals that these states do not satisfy any critical requirements, state G_2 fails only in the shape collapse and crackling noise checks, presenting appropriate power laws and autocorrelations. Most importantly, the activity is autocorrelated with correlation time $\tau_{corr} = (15.70 \pm 0.68)\ s$ and branching parameter $m = 0.9926 \pm 0.0003$. Considering the generality of the latter analysis, supported by its spatial subsampling invariance, and the partial agreement to the other statistical requirements, the network can be considered at least close to criticality in state G_2 also from a global point of view. It is worth mentioning that we have reported the thorough and detailed study on local criticality between electrode pairs by considering a single sample for clarity of presentation. However, similar considerations hold when considering different samples. An example of a study on a different network with similar fabrication parameters is reported in Supplementary Figure S9 (Supporting Information) and extensively commented in Supplementary Note S2 (Supporting Information).

A close comparison among all criticality matrices discloses three main deductions: *i)* local critical dynamics can arise even if the network does not show global criticality as a whole; *ii)* the state showing two-terminal dynamics closest to global criticality is characterized by the largest number of local critical interactions; *iii)* the number of critical electrode couples is maximized when the network is poised to the highest conductance plateau observed during voltage sweep (i.e., the highest conductance plateau observed before the linear increase of G as a function of voltage, as the case of G_2). Notice that, although the plateau-like behavior followed by a smoother conductance growth is a common feature observed in all the networks structurally close to the percolation onset (examples in Supplementary Figure S10, Supporting Information), different networks have been observed to maximize local critical couples at different conductance plateaus. This is expected to be related to the intrinsic network-to-network topological variations arising during the self-assembly process. In any case, results show that local dynamical behavior and critical dynamics are not only influenced by the initial NWN topology, but also by the electrically induced potentiation which modulates the network connectivity and the resulting avalanche dynamics.

2.4. Network Criticality and Computing Capabilities

2.4.1. Nonlinear Transformation Task

NWNs have been shown in the literature to satisfy the main requirements for the implementation of the *in material* reservoir computing paradigm, where the network acts as a physical reservoir able to extract relevant features of the input signal, as shown by implementing various complex tasks such as pattern classification, MNIST handwritten digits recognition, speech recognition, Mackey–Glass forecasting, *n*-back task and nonlinear transformation task (NLT).[26,36,37] This last task, NLT, was here chosen to investigate the relationship between local critical dynamics and computing capabilities in NWNs, since it is widely used as a benchmark for studying the information processing in a physical network. For this purpose, the network was programmed to state G_2, the closest to global criticality and the one with the largest number of local critical interactions, as shown in the previous section. The NLT task was performed in the standard reservoir computing scheme[56] as shown in **Figure 5a**: a sinusoidal voltage waveform is forced to the network between bias and ground electrodes, while reservoir outputs are read simultaneously from the floating voltage electrodes and fed to a linear regression readout layer for target waveforms prediction. In these terms, information processing occurs by exploiting the network dynamical response to a time-varying input signal superimposed to the sustained voltage exploited to maintain the desired state (operating state). In this framework, it is important to remark that SOC can be defined only in the steady state and, thus, cannot be evaluated during the task execution. However, we analyzed in the following the influence of performing information processing in critical or non-critical operating states. In these terms, performing information processing in a critical operating state results in exploiting network dynamics near criticality.

For the NLT task, four target waveforms were chosen: square wave, sawtooth, cosine wave, and doubled-frequency sine wave. The 1 Hz input sinewave is applied immediately after the end of the constant stimulation shown in Figure 4d, without removing the voltage and superimposing the sine as a perturbation of the sustaining bias, operating so in the dynamical conditions described in Section 2.2.

Figure 5b reports the applied voltage waveform together with the output floating voltages (centered in the input mean value by proper translation). Each output is a transformation of the input sine with different degrees of nonlinearity, depending on the dynamics observed in that specific network region, as confirmed also by the Lissajous curves reported in Supplementary Figure S11 (Supporting Information). In particular, in Figure 5b it can be observed that: *i)* areas electrically close to the bias (electrodes 5, 9, 14, 15 in green colors) produce linear transformations of the signal, slightly downscaling the sinewave amplitude; *ii)* weakly active electrodes (electrodes 2–4, 8, 11–13 in brown/gray colors) strongly nonlinearly distort the input, producing low amplitudes sawtooth-like shapes (<3 mV, thus hardly visible in Figure 5b without zooming); and *iii)* areas located at the transition between the previous regions (electrodes 6, 7, 10 in red colors), introduce temporal delays in the input signal (0.14 s, 0.19 s, and 0.09 s, respectively), still preserving sinewave shape and periodicity. The same information (with the same color groups of Figure 5b to facilitate the reading) can be extracted from Lissajous curves in Figure S8 (Supporting Information), where linear, noisy, and circular plots are respectively associated with the three groups previously identified. Remarkably, the last group of electrodes (6, 7, 10) is the same one that establishes most of the local critical interactions in the NWN (Figure 4f), thus suggesting in this case

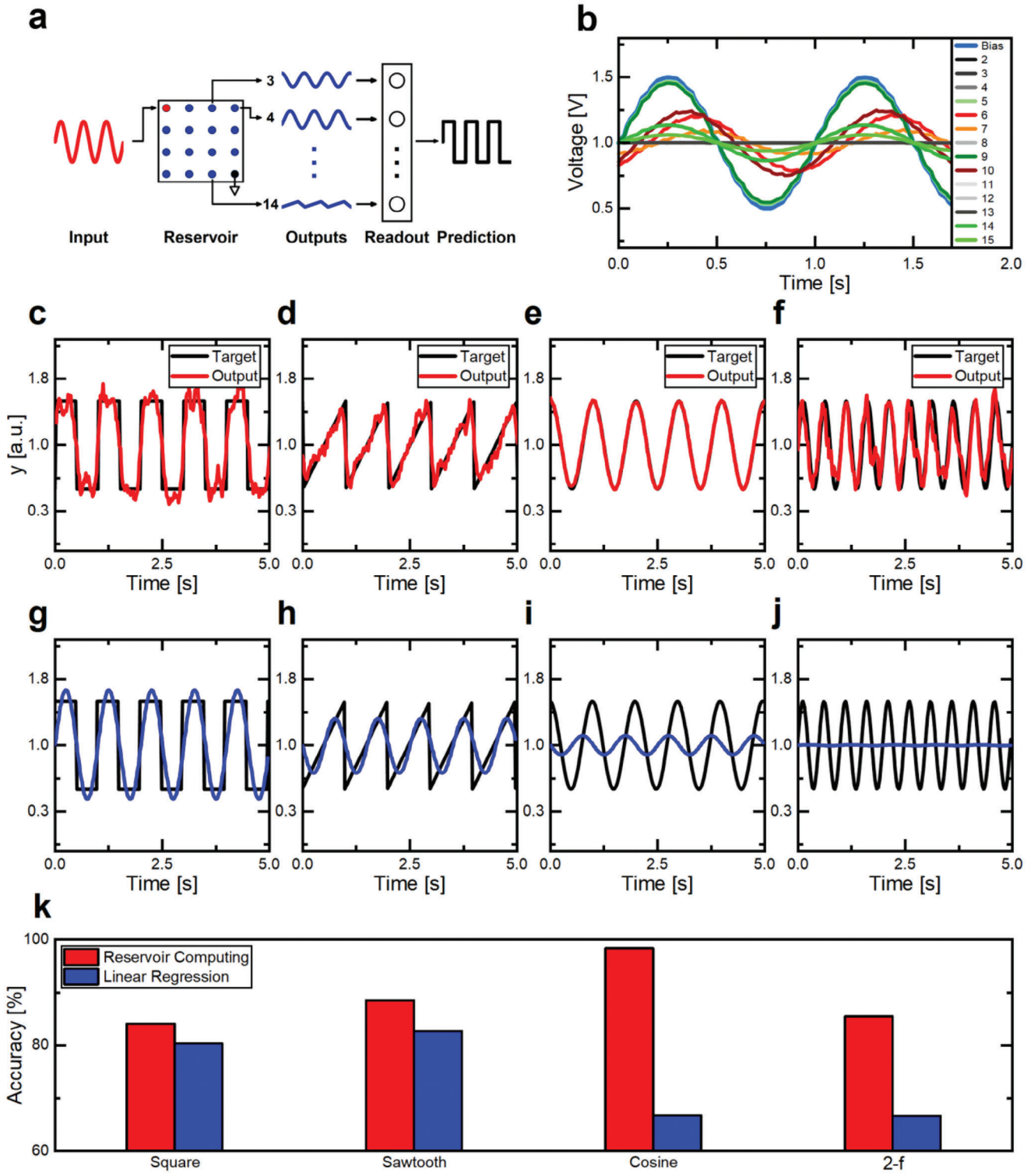

Figure 5. NLT task results. a) Conceptual representation of the Reservoir Computing scheme for the implementation of the NLT task. Input voltage waveform is forced between bias (red dot) and reference (black dot) electrodes while floating output voltages (blue dots) are recorded for probing the reservoir state. NWN outputs are then fed to the linear regression readout layer for target prediction. b) Voltage temporal evolution for input (blue) and nonlinearly transformed output signals. c–f) Target waveforms and RC task results, showing good prediction for the whole set of targets. g,h) Task results with linear regression only. Predicted waveforms (blue) do not reproduce any of the target waveforms (black) features. f) Task performance comparison between reservoir mediated (red) and basic linear regression (blue) implementations, evidencing a significant accuracy gain for temporal transformations (cosine and 2–f).

a correlation between local critical dynamics and signal delay in the network. It must be noted that, despite the steady state conductance signal is subjected to frequent high-magnitude spikes (Supplementary Figure S7, Supporting Information), the sinusoidal input makes the network conductance periodically jump between stable states (Supplementary Figure S12, Supporting Information). In this regime, spikes have been observed not to have a detrimental effect on task performance.

After training the readout layer with linear regression (details in Experimental Section), the output waveforms (red curves in Figure 5c–f) correctly follow all the target curves (black), especially in the cosine transformation (Figure 5e), where the accuracy reaches 98%. The latter result benefits from the delay introduced by the intrinsic network nonlinearities in the output features, particularly on electrode 7 where the shift is almost of a quarter of the period, resulting in directly synchronized to the target waveform. On the other hand, Figure 5g–j shows the same task reconstructions obtained by transforming the input directly through linear regression, i.e., without the NWN as a physical reservoir: it is clear that in this case, the predicted waveforms (blue curves) do not reproduce any key feature of the specific target waveforms (black). A direct comparison between the reconstruction accuracies in the two cases is reported in Figure 5k, where the strong impact due to reservoir dynamics is shown, with accuracy higher than 80% for all the targets and remarkable gain for temporal transformations (cosine and 2-f) that, as expected, are the most complex to perform with only linear methods.

2.4.2. Influence of Local Dynamics on Computing Accuracy

For better elucidating the effect of local dynamics on task performance, a set of differential output features is produced with the same procedure used for the creation of the criticality matrix (paragraph 2.2, third column of Figure 4), and the NLT task is performed feeding this new set of signals to the readout layer. Note that task performance is not affected by this manipulation, being the differential set composed of linear combinations of the original one. Successively, the relevance of each feature is evaluated by assigning it a score proportional to signal significance through an *F*-test for each target waveform (details in Experimental Section), a widely used procedure for feature selection in the framework of machine learning.[59] The full set of scores is reported in Supplementary Figure S13 (Supporting Information), together with the matrices of feature amplitudes and local criticality. Their comparison for square wave and sawtooth reveals a general dependence of relevance on feature magnitudes, while cosine wave and 2-f sine wave high score signals demonstrate a correlation to local critical dynamics. The repeatability of scoring matrices in relation to critical dynamics is shown in Supplementary Figure S9 (Supporting Information) for a different network under multiple recalling of the same conductance state, demonstrating the robustness of this result for both cycle-to-cycle and sample-to-sample variability. Please refer to Supplementary Note S1 (Supporting Information) for a detailed description of differential features production and relative scoring procedure and to Supplementary Note S2 (Supporting Information) for the relative repeatability study.

For deepening the performance dependence on network areas, task accuracy is evaluated as a function of the number of differential signals fed to the readout layer by progressively adding them in decreasing order of scoring. The resulting curves, reported in **Figure 6a**, show a gradual increase followed by a smooth behavior. At the end of the steep transitions, which correspond to 6, 5, 2, and 11 features for square wave, sawtooth, cosine wave, and 2-f sine respectively (Supplementary Figures S14–S17, Supporting Information), accuracies result equal to 83%, 86%, 97% and 87% (Supplementary Figure S18, Supporting Information). These signal sets are sufficient for consistently reconstructing all the targets, demonstrating that a large part of the information required for task execution is mainly carried by a limited number of network outputs. The electrodes involved in their generation are a limited fraction of the whole, with specific spatial distributions dependent on the specific NLT task (Figure 6b–e). For square wave prediction (Figure 6b), regions of very high and very low voltage (bright and dark pixels in the voltage map) are required for correct reconstruction (except for electrode 7), while sawtooth transformation (Figure 6c) relies mainly on low voltage areas. Cosine wave prediction (Figure 6d) requires the lowest number of electrodes: the critical 6 and the bottom border medium conductance ones. Finally, doubling sine frequency transformation (Figure 6e) requires the whole set of nonlinearly transforming electrodes to correctly predict the high-complexity output. Finally, Figure 6f–i shows the histogram reporting the fractions of dominant features exhibiting branching parameters of $m \sim 0$, i.e., non-critical local interaction, and $m \sim 1$, critical, for each target waveform. Remarkably, most relevant information for the execution of temporal complex tasks (cosine, 2-f) is mainly carried out by critically coupled areas ($m \sim 1$), while simpler tasks show to rely on non-critical electrodes features ($m \sim 0$) alone (for sawtooth) or on both critical and non-critical (for square wave). These results suggest that, for NWN physical reservoirs, SOC is not correlated to information processing capabilities of the system in all tasks, but mainly for some specific ones. Although Hochstetter et al.[32] demonstrated in simulations that the NWN critical state maximizes NLT task performance for a whole set of target waveforms, the here reported results look in agreement with Cramer et al.[38] experimental observations in neuromorphic chips that show an even detrimental effect of SOC on simplest tasks. More generally, results from multiterminal analysis reveal that the most relevant features for each NLT task are produced by specific network areas. Such unique characteristics may be used for increasing computing accuracy for reducing hardware complexity and power consumption by measuring a reduced subset of outputs. Looking ahead, NWNs could be optimized to locally adapt for specific tasks (substrate configuration[63]), similarly to the brain where cortical areas are specialized for a specific function upon experience. In this perspective, a crucial role would be played by long-term memory (demonstrated on NWNs[47]), but still not exploited for computing and multiple spatiotemporal inputs.

3. Conclusion

In this work, we reported on the study of self-organized criticality in neuromorphic nanowire networks and on its relationship with nonlinear transformation task execution in the

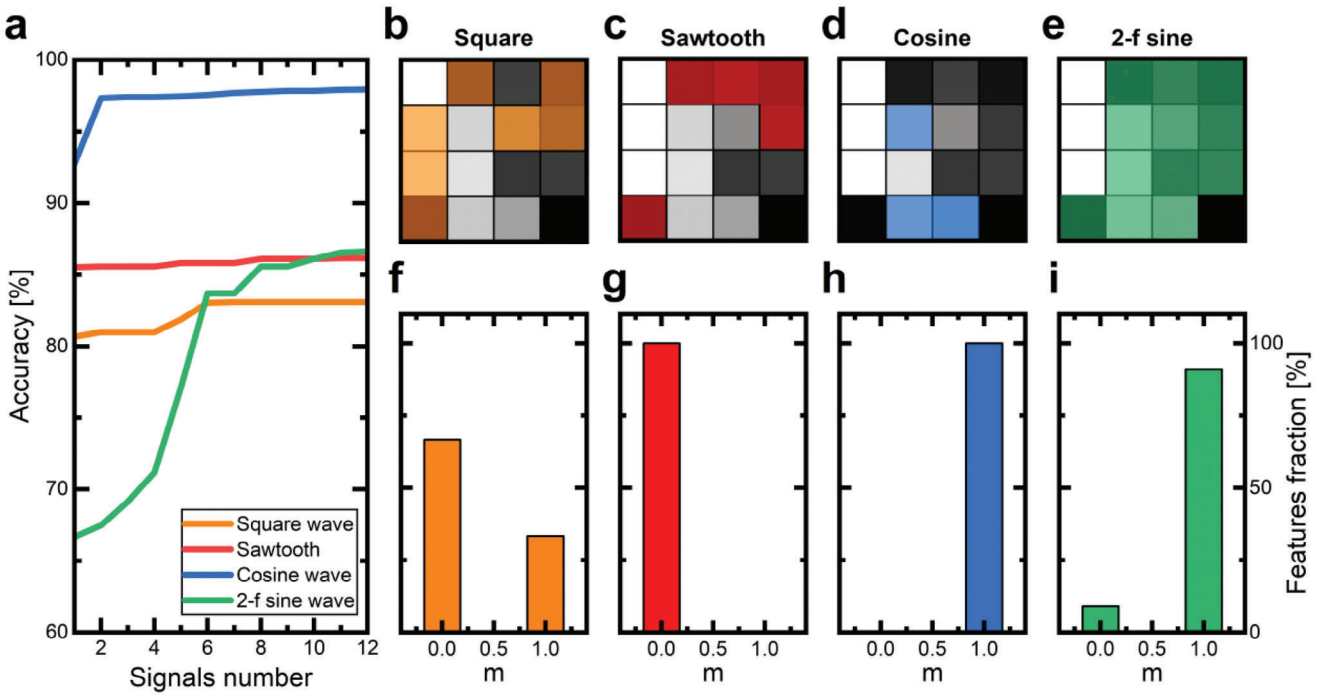

Figure 6. Target-oriented spatial distributions of most relevant outputs. a) Task accuracy behavior by progressive enlargement of readout training set for the top scoring features. b–e) Highlighting of the electrodes necessary for reaching the accuracy plateau for each target prediction and f–i) corresponding histograms of the fraction of relevant electrode couples showing branching parameter m ≈ 0 (non-critical interactions) and m ≈ 1 (critical interactions) for each target waveform.

framework of *in materia* reservoir computing. Multiterminal characterizations demonstrated, in parallel to the emergence of the two-terminal global criticality, that *local* critical dynamics can be revealed among specific network areas. We demonstrated the possibility of electrically programming the network to multiple conductance states, each resulting in a different response in terms of the spatial distribution of the electric field and current flow across the network and local critical interactions between electrodes. Network nonlinear processing was assessed by benchmarking the NLT task, whose results showed the capability of the system to outperform standard linear regression, particularly when temporal transformations are needed. Differently from the most common hypothesis of criticality being beneficial for every class of tasks, features scoring revealed that local critical dynamics are correlated to the generation of features that are relevant mainly for specific target predictions, namely the same ones where the NWN reservoir outperforms linear regression alone. On the contrary, the relevant outputs for simpler tasks are mainly generated by non-critical electrode couples. Finally, the possibility of correctly reconstructing each target with a reduced subset of reservoir outputs with specific properties was demonstrated. This behavior resembles the functional specialization of the different cortical areas in the brain. All these concepts can be extended to multiterminal nanoparticle and nanogranular networks where similar collective resistive switching phenomena are involved. Finally, the understanding of the relationship between network electrical programmability, critical dynamics, and task-oriented relevant features, together with the possibility of performing each task by probing selected network areas only, represents an important step toward the optimization of physical reservoirs and the reduction of RC architecture complexity.

4. Experimental Section

Device Fabrication: Nanowire networks have been produced by drop-casting a dispersion of nanowires onto a ≈1.2 × 1.2 cm^2 SiO_2 insulating substrate for two-terminal experiments and a ≈1 × 1 cm^2 quartz for multiterminal ones. Ag NWs have been purchased by Sigma-Aldrich with a length of 20–50 µm and a diameter of ≈115 nm suspended in isopropyl alcohol. The networks for two-terminal characterization have been fabricated with a drop of 20 µl volume and an NW concentration of ≈0.13 mg mL^{-1} for the sample with $\langle G \rangle = 0.22\ G_0$ and of ≈0.18 mg mL^{-1} for the one with $\langle G \rangle = 73.38\ G_0$. Next, rectangular Au electrodes of area ≈0.3 × 1.2 mm^2 have been deposited through RF sputtering deposition and hard masking patterning. Concerning the multiterminal characterization, the sample has been produced by casting a drop of 13.8 µl volume and a concentration of 1.31 mg ml^{-1} without electrode deposition. The network morphology complexity has been verified by means of a FEI Inspect F Scanning Electron Microscope (SEM).

Electrical Characterization: Two-terminal electrical characterization has been carried out in ambient air in a closed system with a controlled temperature fixed at 303 K by a thermocouple contacting the sample substrate and controlled through a Lake Shore 331 temperature controller. Electric measurements have been performed by means of a Keithley 6430 SourceMeter with a preamplifier, connected to facing electrodes distant ≈7 mm and located at the edges center. The voltage source has been set in the 20 V range, while the current has been measured in auto range mode with a Number of Power Line Cycles (NPLC) equal to 1 and a sampling rate of ≈2.3 Hz. A constant voltage of 0.1 V magnitude has been applied for more than 6 h and a measurement interval of 14 000 s has been selected after 7730 s to ensure network stabilization. Multiterminal

characterization has been carried out by contacting the sample with a 16-electrode square grid with 3 mm inter-electrode spacing, 500 µm distance from sample edges, and probe needles of 50 µm diameter. In this setup, the electrical contact is established by springs producing vertical forces that press the electrodes toward the NWs, as discussed in previous works.[43,61] Voltage application, current recording, and floating voltage measurements were performed by means of an ArC TWO board, which embeds 64 parallel source measure units (SMUs).[62] A detailed analysis of the setup, instrumentation, and protocols for multi-electrode measurements is reported in the previous work.[45] Programing voltage ramps have been applied with a sweep rate $SR = 60\ mV\ s^{-1}$ in a program and verify approach, where the 1 V sustaining voltage was triggered after 5 conductance points overcoming selected thresholds, namely 0.4 G_0 for state G_1, 0.8 G_0 for state G_2 and 1.8 G_0 for state G_3. In the constant voltage phase, measurements have been acquired with a sampling rate of ≈50 Hz for 100s. The first 2 s have been excluded from the analysis to avoid transitory influences.

Criticality Analysis: The LOD value for events detection has been evaluated by selecting the extreme of the derivative interval showing to best fit a Gaussian distribution. The Kolmogorov-Smirnov (KS) test was used for determining the *p*-values of all the zero-centered data subsets, where the maximum p-value identifies the population with the highest probability of being Gaussian distributed. The power-law fitting of IEI autocorrelation has been performed by means of the nonlinear least-square method. The activity autocorrelation function has been evaluated through the multiple-regression (MR) estimation deeply described by Wilting et al.[48] In detail, the ACF value at lag k has been obtained by performing linear regression between all the activity pairs of k lag. The branching parameter *m* has been obtained by least-square fitting of the ACF curve and validated with four statistical criteria that permit to rejection of overestimated values, as described in the same work. The criticality assessment has been carried out by exploiting the commonly used procedure described by Marshall et al., which involves doubly truncated power-law fittings by means of maximum-likelihood estimation, shape collapsing method, and Monte Carlo based uncertainty evaluations.[63] Finally, the uncertainty for crackling noise critical exponent has been evaluated by applying the law of propagation of uncertainty to Equation 5.

Nonlinear Transformation Task Implementation: The nonlinear transformation task has been implemented by applying a sinusoidal voltage to the NWN with a mean value of 1 V, an amplitude of 500 mV, and a frequency of 1 Hz for 8 periods. System response has been recorded simultaneously from all the 16 electrodes with a sampling rate of ≈50 Hz. To ensure network stabilization, the first 3 periods have been discarded and the NLT has been performed on the last 5 periods. The output floating voltage has been smoothed with a 10 points moving average and a software linear regression readout layer was used for the training of each target waveform. As previously done by Fu et al. for the NLT task, the accuracy has been evaluated as 1 – RNMSE, where RNMSE is the root-normalized mean square error (Equation 8).[56] Here, $T(t_n)$ and $y(t_n)$ represent respectively the target value and the reconstructed output at time t_n while N is their total number of points.

$$RNMSE = \sqrt{\frac{\sum_{n=1}^{N}[T(t_n) - y(t_n)]^2}{\sum_{n=1}^{N}[T(t_n)]^2}} \tag{8}$$

The NLT implementation with differential signals has been performed by feeding to the readout layer only features belonging to the strict upper triangular differential matrix to avoid useless redundancy. Features individual scoring has been carried out by exploiting the MATLAB function *fsrftest* that assigns to each signal a score related to the *p*-value of the *F*-test, according to Equation 9.

$$SCORE = -log\,(p\text{–}value) \tag{9}$$

Supporting Information

Supporting Information is available from the Wiley Online Library or from the author.

Acknowledgements

Part of this work was supported by the European project MEMQuD, code 20FUN06. This project (EMPIR 20FUN06 MEMQuD) has received funding from the EMPIR program co-financed by the Participating States and from the European Union's Horizon 2020 research and innovation program. This work has been supported by NEURONE, a project funded by the European Union - Next Generation EU, M4C1 CUP I53D23003600006, under program PRIN 2022 (prj code 20229JRTZA). Part of this work has been carried out at Nanofacility Piemonte INRiM, a laboratory supported by the "'Compagnia di San Paolo"' Foundation, and at the QR Laboratories, INRiM. The authors thank Mr. Danilo Serazio (INRIM) and Dr. Alessandro Cultrera (INRIM) for their technical support on the realization of the multiterminal fixture.

Open access publishing facilitated by Politecnico di Torino, as part of the Wiley - CRUI-CARE agreement.

Conflict of Interest

The authors declare no conflict of interest.

Data Availability Statement

The data that support the findings of this study are available on Zenodo (https://doi.org/10.5281/zenodo.14938156).

Keywords

emerging dynamics, neuromorphic nanowire networks, nonlinear transformations, reservoir computing, self-organized criticality, self-organizing systems

Received: December 5, 2024
Revised: February 7, 2025
Published online: March 3, 2025

[1] P. Bak, C. Tang, *J. Geophys. Res.* **1989**, *94*, 15635.
[2] E. T. Lu, R. J. Hamilton, *Astrophysical Journal, Part 2 – Letters* **1991**, *380*, L89.
[3] J. A. Scheinkman, M. Woodford, *Am Econ Rev* **1994**, *84*, 417.
[4] D. Plenz, E. Niebur, *Criticality in Neural Systems,Wiley* **2014**, *9783527411047*.
[5] J. M. Beggs, D. Plenz, *J. Neurosci.* **2003**, *23*, 11167.
[6] W. L. Shew, H. Yang, T. Petermann, R. Roy, D. Plenz, *J. Neurosci.* **2009**, *29*, 15595.
[7] N. Friedman, S. Ito, B. A. W. Brinkman, M. Shimono, R. E. L. Deville, K. A. Dahmen, J. M. Beggs, T. C. Butler, *Phys. Rev. Lett.* **2012**, *108*, 208102.
[8] T. Petermann, T. C. Thiagarajan, M. A. Lebedev, M. A. L. Nicolelis, D. R. Chialvo, D. Plenz, *Proc Natl Acad Sci* **2009**, *106*, 15921.
[9] V. Priesemann, M. Valderrama, M. Wibral, L. Van Quyen, *PLoS Comput. Biol.* **2013**, *9*, 1002985.
[10] B. Mariani, G. Nicoletti, M. Bisio, M. Maschietto, R. Oboe, A. Leparulo, S. Suweis, S. Vassanelli, *Front Syst Neurosci* **2021**, *15*, 709677.

[11] W. L. Shew, W. P. Clawson, J. Pobst, Y. Karimipanah, N. C. Wright, R. Wessel, *Nature Physic* **2015**, *11*, 659.
[12] J. M. Beggs, N. Timme, *Front Physiol* **2012**, *3*, 24289.
[13] J. M. Beggs, *Philos. Trans. R. Soc., A* **2008**, *366*, 329.
[14] W. L. Shew, H. Yang, S. Yu, R. Roy, D. Plenz, *J. Neurosci.* **2011**, *31*, 55.
[15] N. Bertschinger, T. Natschläger, *Neural Comput* **2004**, *16*, 1413.
[16] O. Kinouchi, M. Copelli, *Nat. Phys.* **2006**, *2*, 348.
[17] C. Haldeman, J. M. Beggs, *Phys. Rev. Lett.* **2005**, *94*, 058101.
[18] W. Maass, T. Natschläger, H. Markram, *Neural Comput* **2002**, *14*, 2531.
[19] P. E. Latham, S. Nirenberg, *Neural Comput* **2004**, *16*, 1385.
[20] A. Z. Stieg, A. V. Avizienis, H. O. Sillin, C. Martin-Olmos, M. Aono, J. K. Gimzewski, *Adv. Mater.* **2012**, *24*, 286.
[21] S. K. Bose, C. P. Lawrence, Z. Liu, K. S. Makarenko, R. M. J. Van Damme, H. J. Broersma, W. G. Van Der Wiel, *Nat. Nanotechnol.* **2015**, *10*, 1048.
[22] H. Tanaka, M. Akai-Kasaya, A. Termehyousefi, L. Hong, L. Fu, H. Tamukoh, D. Tanaka, T. Asai, T. Ogawa, *Nat. Commun.* **2018**, *9*, 2693.
[23] T. Chen, J. van Gelder, B. van de Ven, S. V. Amitonov, B. de Wilde, H. C. Ruiz Euler, H. Broersma, P. A. Bobbert, F. A. Zwanenburg, W. G. van der Wiel, *Nature* **2020**, *577*, 341.
[24] G. Martini, E. Tentori, M. Mirigliano, D. E. Galli, P. Milani, F. Mambretti, *Front. Phys.* **2024**, *12*, 1400919.
[25] J. B. Mallinson, S. Shirai, S. K. Acharya, S. K. Bose, E. Galli, S. A. Brown, *Sci. Adv.* **2019**, *5*, https://www.science.org/doi/10.1126/sciadv.aaw8438.
[26] A. Loeffler, A. Diaz-Alvarez, R. Zhu, N. Ganesh, J. M. Shine, T. Nakayama, Z. Kuncic, *Sci. Adv.* **2023**, *9*, https://www.science.org/doi/10.1126/sciadv.adg3289.
[27] A. Diaz-Alvarez, R. Higuchi, P. Sanz-Leon, I. Marcus, Y. Shingaya, A. Z. Stieg, J. K. Gimzewski, Z. Kuncic, T. Nakayama, *Sci. Rep.* **2019**, *9*, 14920.
[28] G. Milano, E. Miranda, C. Ricciardi, *Neural Networks* **2022**, *150*, 137.
[29] F. Caravelli, G. Milano, C. Ricciardi, Z. Kuncic, *Ann. Phys.* **2023**, *535*, 2300090.
[30] K. Montano, G. Milano, C. Ricciardi, *Neuromorphic Computing and Engineering* **2022**, *2*, 014007.
[31] G. Milano, S. Porro, I. Valov, C. Ricciardi, *Adv. Electron. Mater.* **2019**, *5*, 1800909.
[32] J. Hochstetter, R. Zhu, A. Loeffler, A. Diaz-Alvarez, T. Nakayama, Z. Kuncic, *Nat. Commun.* **2021**, *12*, 4008.
[33] C. S. Dunham, S. Lilak, J. Hochstetter, A. Loeffler, R. Zhu, C. Chase, A. Z. Stieg, Z. Kuncic, J. K. Gimzewski, *Journal of Physics: Complexity* **2021**, *2*, 042001.
[34] R. Zhu, S. Lilak, A. Loeffler, J. Lizier, A. Stieg, J. Gimzewski, Z. Kuncic, *Nat. Commun.* **2023**, *14*, 6697.
[35] J. B. Mallinson, J. K. Steel, Z. E. Heywood, S. J. Studholme, P. J. Bones, S. A. Brown, *Adv. Mater.* **2024**, *36*, 2402319.
[36] G. Milano, K. Montano, C. Ricciardi, *J Phys D Appl Phys* **2023**, *56*, 084005.
[37] G. Milano, G. Pedretti, K. Montano, S. Ricci, S. Hashemkhani, L. Boarino, D. Ielmini, C. Ricciardi, *Nat. Mater.* **2021**, *21*, 195.
[38] B. Cramer, D. Stöckel, M. Kreft, M. Wibral, J. Schemmel, K. Meier, V. Priesemann, *Nat. Commun.* **2020**, *11*, 2853.
[39] G. Milano, G. Pedretti, M. Fretto, L. Boarino, F. Benfenati, D. Ielmini, I. Valov, C. Ricciardi, *Advanced Intelligent Systems* **2020**, *2*, 2000096.
[40] G. Milano, A. Cultrera, K. Bejtka, N. De Leo, L. Callegaro, C. Ricciardi, L. Boarino, *ACS Appl. Nano Mater.* **2020**, *3*, 11987.
[41] Y. Sun, B. Gates, B. Mayers, Y. Xia, *Nano Lett* **2002**, *2*, 165.
[42] Y. Sun, Y. Xia, *Adv. Mater.* **2002**, *14*, 833.
[43] G. Milano, F. Raffone, K. Bejtka, I. De Carlo, M. Fretto, F. C. Pirri, G. Cicero, C. Ricciardi, I. Valov, *Nanoscale Horiz* **2024**, *9*, 416.
[44] G. Milano, A. Cultrera, L. Boarino, L. Callegaro, C. Ricciardi, *Nat. Commun.* **2023**, *14*, 5723.
[45] D. Pilati, F. Michieletti, A. Cultrera, C. Ricciardi, G. Milano, *Adv. Electron. Mater.* **2024**, *10*, 2400750.
[46] R. F. Voss, *J Phys A Math Gen* **1984**, *17*, L373.
[47] S. B. Lowen, M. C. Teich, *Phys. Rev. E* **1993**, *47*, 992.
[48] J. Wilting, V. Priesemann, *Nat. Commun.* **2018**, *9*, 2325.
[49] V. Priesemann, M. Wibral, M. Valderrama, R. Pröpper, M. Le Van Quyen, T. Geisel, J. Triesch, D. Nikolić, M. H. J. Munk, *Front Syst Neurosci* **2014**, *8*, 108.
[50] J. P. Sethna, K. A. Dahmen, C. R. Myers, *Nature* **2001**, *410*, 242.
[51] H. G. Manning, F. Niosi, C. Gomes Da Rocha, A. T. Bellew, C. O'callaghan, S. Biswas, P. F. Flowers, B. J. Wiley, J. D. Holmes, M. S. Ferreira, J. J. Boland, *Nat. Commun.* **2018**, *9*, 3219.
[52] K. Christensen, N. R. Moloney, *Complexity and criticality*, *1*, Imperial College Press, London, UK, **2005**
[53] M. A. Muñoz, *Rev. Mod. Phys.* **2018**, *90*, 031001.
[54] W. Wang, M. Laudato, E. Ambrosi, A. Bricalli, E. Covi, Y. H. Lin, D. Ielmini, *IEEE Trans. Electron Devices* **2019**, *66*, 3795.
[55] G. Milano, T. Chakrabarty, C. Ricciardi, presented at, 2023 IEEE Int. Conf. on Metrology for eXtended Reality, Milano, Italy, October, **2023**.
[56] K. Fu, R. Zhu, A. Loeffler, J. Hochstetter, A. Diaz-Alvarez, A. Stieg, J. Gimzewski, T. Nakayama, Z. Kuncic, presented at, 2020 Int. Joint Conf. on Neural Networks (IJCNN), Glasgow, UK, July, **2020**.
[57] G. Milano, M. Agliuzza, N. De Leo, C. Ricciardi, presented at, Proc. of the Int. Joint Conf. on Neural Networks, Padua, Italy, July, **2022**.
[58] E. C. Demis, R. Aguilera, K. Scharnhorst, M. Aono, A. Z. Stieg, J. K. Gimzewski, *Jpn. J. Appl. Phys.* **2016**, *55*, 1102B2.
[59] N. Omer, F. Elssied, O. Ibrahim, A. H. Osman, *Res. J. Appl. Sci., Eng. Technol.* **2014**, *7*, 625.
[60] M. Dale, S. O'Keefe, A. Sebald, S. Stepney, M. A. Trefzer, *Nat Comput* **2021**, *20*, 205.
[61] A. Cultrera, G. Milano, N. De Leo, C. Ricciardi, L. Boarino, L. Callegaro, *Scientific Report* **2021**, *11*, 1.
[62] P. Foster, J. Huang, A. Serb, S. Stathopoulos, C. Papavassiliou, T. Prodromakis, *Sci. Rep.* **2022**, *12*, 13912.
[63] N. Marshall, N. M. Timme, N. Bennett, M. Ripp, E. Lautzenhiser, J. M. Beggs, *Front Physiol* **2016**, *7*, 452.